

See discussions, stats, and author profiles for this publication at: <https://www.researchgate.net/publication/260749445>

Combined Surface and Electrochemical Study of the Lithiation/Delithiation Mechanism of the Iron Oxide Thin-Film Anode for Lithium-Ion Batteries

ARTICLE *in* THE JOURNAL OF PHYSICAL CHEMISTRY C · OCTOBER 2013

Impact Factor: 4.77

CITATIONS

2

READS

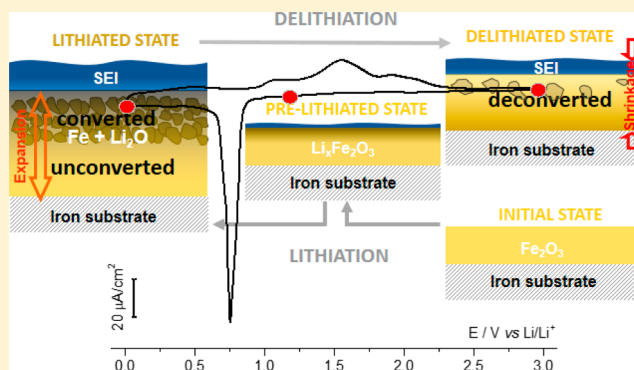
37

Combined Surface and Electrochemical Study of the Lithiation/Delithiation Mechanism of the Iron Oxide Thin-Film Anode for Lithium-Ion Batteries

Bingbing Tian, Jolanta Światowska,* Vincent Maurice, Sandrine Zanna, Antoine Seyeux, Lorena H. Klein, and Philippe Marcus

Laboratoire de Physico-Chimie des Surfaces, Chimie ParisTech - CNRS (UMR 7045), Ecole Nationale Supérieure de Chimie de Paris, 11 rue Pierre et Marie Curie, 75005 Paris, France

ABSTRACT: Iron oxide (mostly $\alpha\text{-Fe}_2\text{O}_3$) model thin-film electrodes were prepared by thermal oxidation of pure metal iron substrates at $300 \pm 5^\circ\text{C}$ in air and used for comprehensive investigation of the lithiation/delithiation mechanisms of anode material undergoing an electrochemical conversion reaction with lithium ions. Surface (X-ray photoelectron spectroscopy (XPS) and time-of-flight secondary ion mass spectrometry (ToF-SIMS)) and electrochemical (cyclic voltammetry (CV) and electrochemical impedance spectroscopy (EIS)) analytical techniques were combined. The results show that intercalation of Li in the Fe_2O_3 matrix and solid electrolyte interphase (SEI) layer formation both precede conversion to metallic iron and Li_2O upon lithiation. Depth profile analysis evidences stratification of the converted thin-film electrode into fully and partially lithiated outer and inner parts, respectively, due to mass transport limitation. The SEI layer has a stable composition (Li_2CO_3 with minor ROCO_2Li) but dynamically increases/decreases in thickness upon lithiation/delithiation. Conversion, proceeding mostly in the outer part of the electrode, causes material swelling accompanied by SEI layer thickening. Upon delithiation, lithium is trapped in the deconverted electrode subjected to shrinking, and the SEI layer mostly decomposes and reduces in thickness after deconversion. The nonreversibility of both conversion and surface passivation mechanisms is demonstrated.



1. INTRODUCTION

Lithium-ion batteries (LiBs) are widely used for portable electronic devices and have become the most competitive candidate for electric vehicles due to numerous advantages, such as light weight and high energy and power density. Graphite, the currently used commercial anode material, has a limited theoretical specific capacity (372 mAh g^{-1}) and presents safety issues. Much effort is made to develop new types of anode materials such as transition metal oxides (e.g., CoO , Co_3O_4 , NiO , CuO , Cu_2O , FeO , Fe_2O_3 , Fe_3O_4 , Cr_2O_3),^{1–4} lithium-based alloys (e.g., Li-Si , Li-Sn),^{6–13} or other metal binary alloys (e.g., Si-based and $\text{Sn-based intermetallics}$)^{14–18} that present high interest due to high theoretical capacities and improved safety.

Iron oxides (including FeO , Fe_2O_3 , and Fe_3O_4) have attracted much interest.^{1,4,19–21} Among them, $\alpha\text{-Fe}_2\text{O}_3$ (hematite) and spinel Fe_3O_4 (magnetite) are very promising as anode materials owing to their high capacity, environmental friendliness, abundance, and low cost.^{4,22} However, they are not used in commercial LiBs due to capacity fading upon cycling, high operating potentials, and poor lithiation/delithiation kinetics. These limitations are all related to the unique lithium storage mechanism, the so-called “conversion reaction”, by which formation of amorphous lithium oxide (Li_2O) and iron metal occurs.¹

In recent years, efforts have been made to improve the electrochemical properties of iron oxides as anode material. However, in these studies, iron oxides were widely investigated as powder and/or nanostructured materials for the purpose of improving electrochemical performance.^{4,22,23} Only a few studies focused on the preparation and electrochemical performance of thin-film electrodes without any conducting additives and binder,^{23,24} and to our knowledge, no study used the thin-film approach to address the conversion mechanism and the formation of the solid electrolyte interphase (SEI) layer in detail. Thin-film electrodes without conducting additives and binder are more suitable for fundamental studies of energy storage mechanisms and interfacial modifications than powder electrodes since they are better suited for the application of surface and interface analytical methods.

Here we report on iron oxide thin-film electrodes prepared via simple thermal oxidation of an iron metal substrate used as a current collector with the objective to investigate thoroughly the conversion mechanism and the SEI-induced surface passivation. Surface and depth profile analysis of the lithiated and delithiated

Received: June 29, 2013

Revised: September 20, 2013

Published: September 24, 2013

thin-film electrodes was performed with X-ray photoelectron spectroscopy (XPS) and time-of-flight secondary ion mass spectrometry (ToF-SIMS). Cyclic voltammetry (CV) in a half cell with 1 M $\text{LiClO}_4\text{-PC}$ as electrolyte was used to control the electrochemical lithiation/delithiation process, and electrochemical impedance spectroscopy (EIS) was applied to characterize the charge transfer process. Formation and stability of the SEI layer and the conversion/deconversion mechanism are discussed for the first cycle of lithiation/delithiation of iron oxide used as anode material for LIBs, and some preliminary electrochemical studies of the cycling performance are presented. More detailed analysis of the cycling-induced modifications of the electrode and its passivation film as well as the aging mechanisms will be discussed in a forthcoming paper.

2. EXPERIMENTAL SECTION

2.1. Preparation of Iron Oxide Thin Films. Pure (99.99 wt %) iron plates (1 mm thick) were purchased from Goodfellow and then cut into square ($8 \times 8 \text{ mm}^2$) substrate samples. The surfaces were prepared by mechanical polishing with diamond spray down to $1/4 \mu\text{m}$ and then rinsed in ultrasonic baths of acetone, ethanol, and Millipore water (resistivity $>18 \text{ M}\Omega \text{ cm}$) for 2 min and dried in a flow of compressed air.

Iron oxide thin films were prepared by thermal oxidation in air. The samples were placed in a quartz tube that could be inserted in a cylindrical oven set to a temperature of $300 \pm 5^\circ\text{C}$. The samples were placed in the prethermalized oven for 5 min, and then the quartz tube was quenched with 0°C water for cooling. The average thickness of the pristine oxide thin films was 85–95 nm as estimated from XPS depth profile analysis. Raman spectroscopy (Horiba Xplora system, Ar^+ laser, $\lambda = 532 \text{ nm}$) was employed for phase identification of the thermal oxide.

2.2. Electrochemical Measurements. All electrochemical measurements (CV and EIS) were performed in an Ar-filled glovebox (Jacomex) with H_2O and O_2 contents lower than 1 ppm. A homemade three-electrode glass cell similar to typical commercial cells was used with the iron oxide thin film (prepared as described above) as a working electrode and two Li foils (Sigma-Aldrich) used as reference and counter electrodes. The surface of the counter electrode was around 2 cm^2 . All potentials hereafter are given versus Li/Li^+ . The cell was operated at room temperature using an Autolab (AUT30) electrochemical workstation. The geometrical working electrode area was delimited to 0.28 cm^2 by a Viton O-ring. The electrolyte was 1 M LiClO_4 in propylene carbonate (1 M $\text{LiClO}_4\text{-PC}$, Sigma-Aldrich). Cyclic voltammograms were recorded in the potential range 0.01–3.0 V at a scanning rate of 0.2 mV s^{-1} , starting from OCP ($\sim 3.0 \text{ V}$) into the cathodic direction. For EIS measurements, the frequency range was 10 mHz to 1 MHz, and the potential perturbation was 5 mV. The cell was kept at selected potential value for more than 30 min before performing EIS, and the equilibrium of the cells was deemed to be reached when the change of voltage was less than 0.01 V in 10 min.

For surface and depth profile analysis the thin films were electrochemically treated at various stages of the first cycle. After scanning the potential to the selected value, the cell was disassembled, and the samples were rinsed with acetonitrile (99.8%, Sigma-Aldrich) and dried with Ar flow. The samples were then transferred directly from the glovebox to the ultrahigh vacuum XPS analysis chamber.²⁵ Thereafter, they were transferred in an airtight vessel under argon atmosphere from the XPS to the ToF-SIMS system.

2.3. X-ray Photoelectron Spectroscopy (XPS). XPS analysis was carried out on a VG ESCALAB 250 spectrometer with a UHV preparation chamber directly connected to the glovebox. Base pressure during analysis was 10^{-9} mbar. An Al $K\alpha$ monochromatized radiation ($h\nu = 1486.6 \text{ eV}$) was employed as the X-ray source. The take-off angle of the photoelectrons was 90° . Survey spectra were recorded with a pass energy of 100 eV at a step size of 1 eV, and high-resolution spectra of the Fe 2p, O 1s, and C 1s core level and valence band (VB) regions were recorded with a pass energy of 20 eV at a step size of 0.1 eV. The data processing (curve fitting) was performed using the Advantage software provided by Thermo Electron Corporation. An iterative Shirley-type background and Lorentzian/Gaussian peak shape at a fixed ratio of 30/70 were used. Binding energies were calibrated by setting the C 1s hydrocarbon ($-\text{CH}_2-\text{CH}_2-$) component peak at 285.0 eV. XPS depth profiling was performed by combining analysis with Ar^+ sputtering performed in the preparation chamber. A 2 keV Ar^+ sputter beam giving $0.2 \mu\text{A mm}^{-2}$ of sample current yielded a calibrated etching rate of about 2.5 nm min^{-1} . The depth profiles were stopped after etching about 150 nm.

2.4. Time-of-Flight Secondary Ion Mass Spectrometry (ToF-SIMS). Depth profiling was also performed using a ToF-SIMS 5 spectrometer (Ion ToF - Munster, Germany). The operating pressure of the spectrometer was about 10^{-9} mbar. A pulsed 25 keV Bi^+ primary ion source was employed for analysis, delivering 1.2 pA current over a $100 \times 100 \mu\text{m}^2$ area. Depth profiling was carried out using a 1 keV Cs^+ sputter beam giving a 70 nA target current over a $300 \times 300 \mu\text{m}^2$ area. Ion-Spec software was used for acquiring and processing the data. Negative ion depth profiles were recorded for better sensitivity to fragments originating from oxide matrices.

3. RESULTS AND DISCUSSION

3.1. Raman Phase Identification. Figure 1 displays the Raman spectrum of the as-prepared thermal iron oxide thin film.

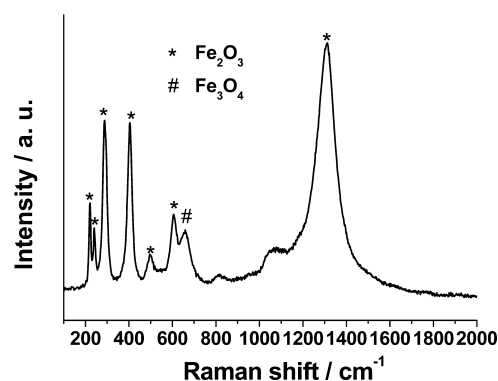


Figure 1. Raman spectra of iron oxide thin film grown by thermal oxidation of pure iron metal at $300 \pm 5^\circ\text{C}$ in air.

There are several peaks in the range of $100\text{--}2000 \text{ cm}^{-1}$. On the basis of reference compounds,^{23,26–28} the spectrum is indicative of a crystalline thin film consisting mostly of the thermodynamically stable $\alpha\text{-Fe}_2\text{O}_3$ (hematite) phase together with Fe_3O_4 (magnetite) in a small amount. The peaks located at 222, 241, 287, 404, 495, 606, and 1313 cm^{-1} all correspond to the $\alpha\text{-Fe}_2\text{O}_3$ phase. They are assigned to two A_{1g} modes (at 222 and 495 cm^{-1}) and five E_g modes (at 241, 287, shoulder near 287, 404, and 606 cm^{-1}). The intense peak at 1313 cm^{-1} is assigned to

two-magnon scattering which arises from the interaction of antiparallel close spin sites.²⁸ The peak at 659 cm⁻¹ can be assigned to an A_{1g} mode of Fe₃O₄ (magnetite). The relative intensities of the peaks at 241, 404, and 1313 cm⁻¹ are much higher than reported in the literature for reference compounds,^{23,28,29} which is indicative of the presence of α -FeOOH (goethite) also supported by the XPS data presented below.

3.2. Cyclic Voltammetry (CV). Figure 2(a) shows the CV corresponding to the first lithiation/delithiation cycle of the iron

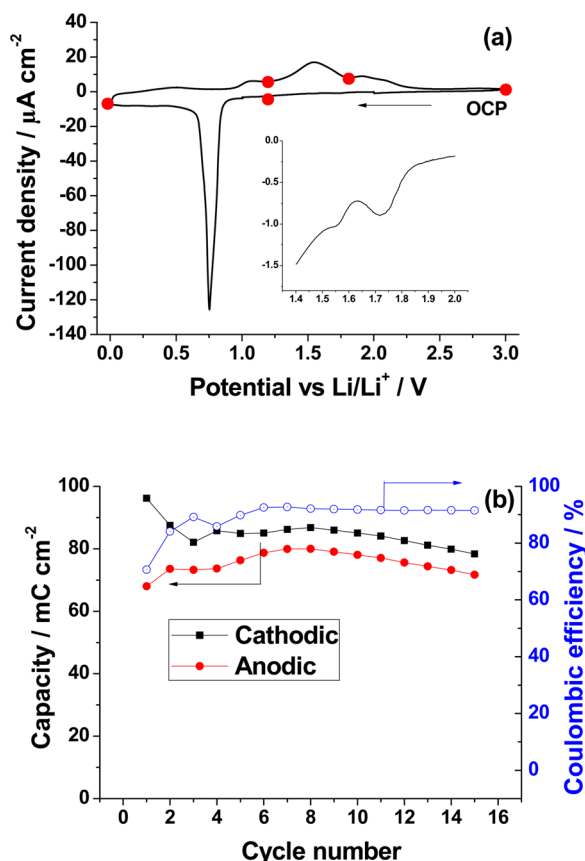
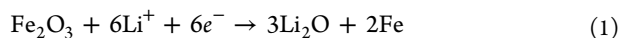
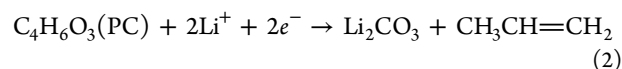


Figure 2. (a) Cyclic voltammogram (CV) of first lithiation/delithiation of iron oxide thin-film electrode in 1 M LiClO₄-PC in the 0.01–3.0 V potential range (scan rate of 0.2 mV s⁻¹). The inset shows the magnified cathodic peak at 1.7 V. Points on the curves indicate the selected potentials for XPS, ToF-SIMS, and EIS analysis. (b) Anodic and cathodic charges and Coulombic efficiency calculated from 15 lithiation/delithiation cycles performed by cycling voltammetry.

oxide thin-film electrode. Only visible in the inset, the CV shows a small cathodic peak at about 1.7 V followed by a moderate cathodic current increase until 1 V. This small cathodic peak followed by increased cathodic current has been assigned to the process of Li intercalation into the Fe₂O₃ matrix to form Li_xFe₂O₃ (0 < x ≤ 2), as shown by in situ X-ray diffraction.²¹ The sharp and intense cathodic peak located at 0.75 V corresponds to the process of electrochemical reduction of lithium with iron oxide (mainly α -Fe₂O₃), as described by eq 1^{19–21,30–33}



This cathodic peak has also been assigned to the electrochemical formation of the SEI layer by reductive decomposition of the electrolyte on the surface of other conversion-type electrode material such as Cr₂O₃, on which the reaction is expected to be similar to that on Fe₂O₃. The reaction is described by eq 2⁵



In the anodic scan, there is a broad peak centered at 1.55 V, which is related to the deconversion process of Li₂O with metallic iron (Fe⁰) and can be described by eq 3

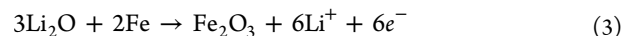


Figure 2(b) shows the cycling performance of the iron oxide thin-film electrode calculated from integrals of the cathodic and anodic processes of 15 cycles (CVs). The cathodic capacity (96 mC cm⁻²) is much higher than anodic capacity (68 mC cm⁻²) in the first CV cycle, which indicates high initial irreversible capacity related to electrolyte decomposition and formation of the SEI layer and possibly incomplete reversible deconversion as discussed further on. The reversible capacity for the cathodic process slightly decreases with cycle number and reaches 83% of the initial value at the 15th cycle. The low Coulombic efficiency (~70%) observed initially increases and stabilizes at 92% after 15 cycles. More details concerning the cycling performance of thin-film iron oxide electrode and the morphological and chemical modifications induced by repeated electrochemical lithiation/delithiation will be discussed in a forthcoming paper.

The potential values selected for EIS, XPS, and ToF-SIMS analyses at different stages of the first lithiation (cathodic) and delithiation (anodic) process are marked in Figure 2(a). They are: 1.2 V (before cathodic peak), 0.01 V (at cathodic vertex potential), 1.2 V (before anodic peak), 1.8 V (after anodic peak), and 3.0 V (at anodic vertex potential).

3.3. Electrochemical Impedance Spectroscopy (EIS). As widely discussed in EIS studies of intercalation/deintercalation-type materials,^{34–37} a semicircle in the high-frequency spectral region relates to charge transfer resistance, and a straight line at 45° against the real axis in the low-frequency range corresponds to a Warburg impedance, which is valid in the semi-infinite diffusion conditions.³⁸ However, for conversion-type Fe₂O₃, a phase change characterizes the lithiation/delithiation process.^{21,23} So it seems that some impedance parameters (such as Warburg impedance describing solid-state diffusion of Li⁺ in α -Fe₂O₃) may not be as meaningful as for intercalation/deintercalation-type materials because of this phase change.

Figure 3 shows the electrochemical impedance spectra (Nyquist plots) of the electrode at the various selected stages of the first lithiation/delithiation cycle. The potential values in parentheses are the equilibrium values reached before the EIS measurement for relaxed cells. The high electrolyte resistance (~156 Ω cm²) observed for all analyzed samples is due to the geometrical configuration of the three-electrode cell (i.e., large distance between working, reference, and counter electrodes) and not to poor conductivity of the electrolyte commonly employed in LiB studies. For the pristine sample (at OCP) the EIS shows an almost straight line without any obvious semicircle in the high-frequency region, implying that the system represents only a bulk solution resistance before any lithiation occurs.³⁹ Moreover, the slope of the line is the highest at this stage, which is probably due to finite diffusion in the limited thickness of the unmodified thin-film electrode.

With lithiation, a depressed semicircle appears at high frequency. The presence of one semicircle was also observed in several previous studies performed on the iron oxide electrode.^{23,32,40–42} The varying diameter of the depressed semicircle indicates a gradual increase of a charge transfer resistance from ~14 Ω cm² in the lithiated state at 1.2 V to ~32 Ω cm²

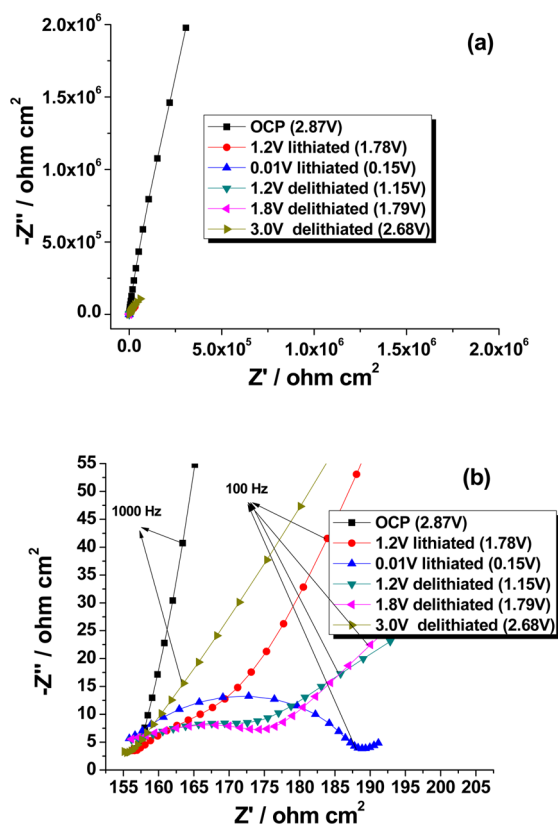


Figure 3. (a) EIS (Nyquist plots) spectra of the iron oxide thin-film electrode at selected potentials in the first lithiation/delithiation cycle in 1 M LiClO₄-PC. (b) Magnified high-frequency region of spectra in (a). Potentials given in brackets are equilibrium values reached at each stage.

in the completely lithiated state at 0.01 V. It is conjectured that this increase is related to the growth of the SEI layer on the thin-film electrode, as previously reported.⁴³ If so, the present data indicate that growth of the SEI layer would be initiated already at 1.2 V before conversion of the electrode, which is confirmed by the XPS data presented below. In the lithiated state at 1.2 V, the straight line with a 45° angle at low frequency indicates semi-infinite diffusion in the not yet converted thin-film electrode. At 0.01 V, the depressed semicircle in the whole frequency range corresponds to the SEI layer dominating the impedance response.

With delithiation, the impedance spectra markedly change. The decreasing depressed semicircles at high frequency are attributed to decomposition of the SEI layer, and the straight lines at low frequency are indicative of diffusion in the deconverting thin-film electrode. At 1.2 V (delithiation state), the charge transfer resistance is about $\sim 20 \Omega \text{ cm}^2$, indicating some partial decomposition of the SEI layer already before deconversion of the thin-film electrode. No further decomposition is observed at 1.8 V after deconversion, suggesting stability of the SEI layer during the main deconversion reaction. It is only at 3.0 V that the semicircle nearly vanishes, indicating further but not complete decomposition of the SEI layer at this stage. At low frequency, only a slightly higher slope is observed at 1.8 V after deconversion, suggesting that the reaction may not be fully reversible at this stage. At 3.0 V, the slope markedly increases but remains lower than for the pristine sample indicating that the electrochemically induced modifications of the electrode are not fully reversible.

3.4. XPS Surface Analysis. The XP C 1s, O 1s, Fe 2p, and Fe 3p-Li 1s core levels and VB region spectra for the pristine iron oxide thin film and samples treated at the selected potentials are shown in Figure 4. Binding energies (E_B), full widths at half-maximum (fwhm), and relative intensity of the component peaks obtained by peak fitting are given in Table 1. For the pristine sample, the C 1s signal is indicative of the carbonaceous contamination routinely observed on oxide surfaces. It is decomposed into one major component at 285.0 eV (C 1s_A) assigned to $-\text{CH}_2-\text{CH}_2-$ bonds and two minor components at 286.5 eV (C 1s_B) and 288.4 eV (C 1s_C) assigned to C-O bonds and O=C (carbonyl) and/or O=C-O (carboxyl) bonds, respectively.^{5,44,45}

The major oxygen component peak at E_B (O 1s_A) = 530.0 eV is attributed to Fe-O bonds in the iron oxide matrix. The minor component at E_B (O 1s_B) = 531.6 eV can be ascribed to surface contamination (C=O bonds and/or O=C-O bonds).^{44,45} This component can also correspond to hydroxyl groups.⁴⁶ These species would originate from iron oxyhydroxide (FeOOH) whose presence is also confirmed by the Fe 2p core level. A third component at E_B (O 1s_C) = 532.8 eV, corresponding to water molecules,⁵ is barely observed on the pristine film.

The Fe 2p spectrum shows the 3/2-1/2 spin orbit doublet. Only the Fe 2p_{3/2} core level peak was fitted for simplicity. It displays five components. The two adjacent peaks (Fe 2p_{3/2B} and Fe 2p_{3/2C}) with a binding energy separation of 1 eV observed at 709.7 and 710.7 eV are assigned to Fe(III) in an oxide matrix (Fe₂O₃ and/or Fe₃O₄).⁴⁶⁻⁴⁸ The peak at 708.3 eV (Fe 2p_{3/2A}) is assigned to Fe(II) in an oxide matrix (in agreement with the Raman spectrum showing the minor presence of Fe₃O₄), and that at 712.2 eV (Fe 2p_{3/2D}) is assigned to Fe(III) in an oxyhydroxide matrix (FeOOH). The minor component at 714.3 eV (Fe 2p_{3/2E}) is attributed to a Fe(II) 2p_{3/2} satellite.⁴⁸ Thus, the Fe 2p_{3/2} core level is consistent with the predominance of α -Fe₂O₃ in the thermally grown oxide film and some presence of Fe(II) oxide (Fe₃O₄) and Fe(III) oxyhydroxide (FeOOH) as concluded from the Raman data. The low intensity of the Fe(II) oxide component can result from the preferential formation of Fe₃O₄ in the inner part of the film, as supported by ToF-SIMS depth profile analysis. The larger intensity of the Fe(III) oxyhydroxide component is consistent with this species concentrated at the oxide thin-film surface and resulting from reaction with water vapor.

After lithiation to 1.2 V, one new C 1s_D component is observed at 289.9 eV and assigned to Li₂CO₃ and/or ROCO₂Li.^{5,44,45} It indicates, in agreement with the EIS data, that the formation of the SEI layer occurs already at this potential although it is mainly expected to be formed at about 0.75 V. The O 1s_A component is shifted to 529.5 eV indicating modification of the oxide matrix, possibly by intercalation of lithium as previously concluded from XRD data.^{20,21} Its attenuation is consistent with growth of the SEI layer. The O 1s_B peak, assigned to carbonates, markedly increases in relative intensity showing SEI layer growth. Its intensity is about 7 times that of the O 1s_D peak at 533.4 eV assigned to Li-alkyl carbonates. This indicates that Li₂CO₃ and ROCO₂Li are the major and minor components of the SEI layer, respectively, already at this initial stage of lithiation.

In the Fe 2p_{3/2} spectrum, the Fe(III)OOH component (Fe 2p_{3/2D}) has vanished, and the Fe(III) oxide component (Fe 2p_{3/2C}) and Fe(II) oxide component (Fe 2p_{3/2A}) have, respectively, decreased and increased in intensity. This is consistent with the formation of Li_xFe₂O₃ ($0 < x \leq 2$) previously observed at this potential.^{21,22}

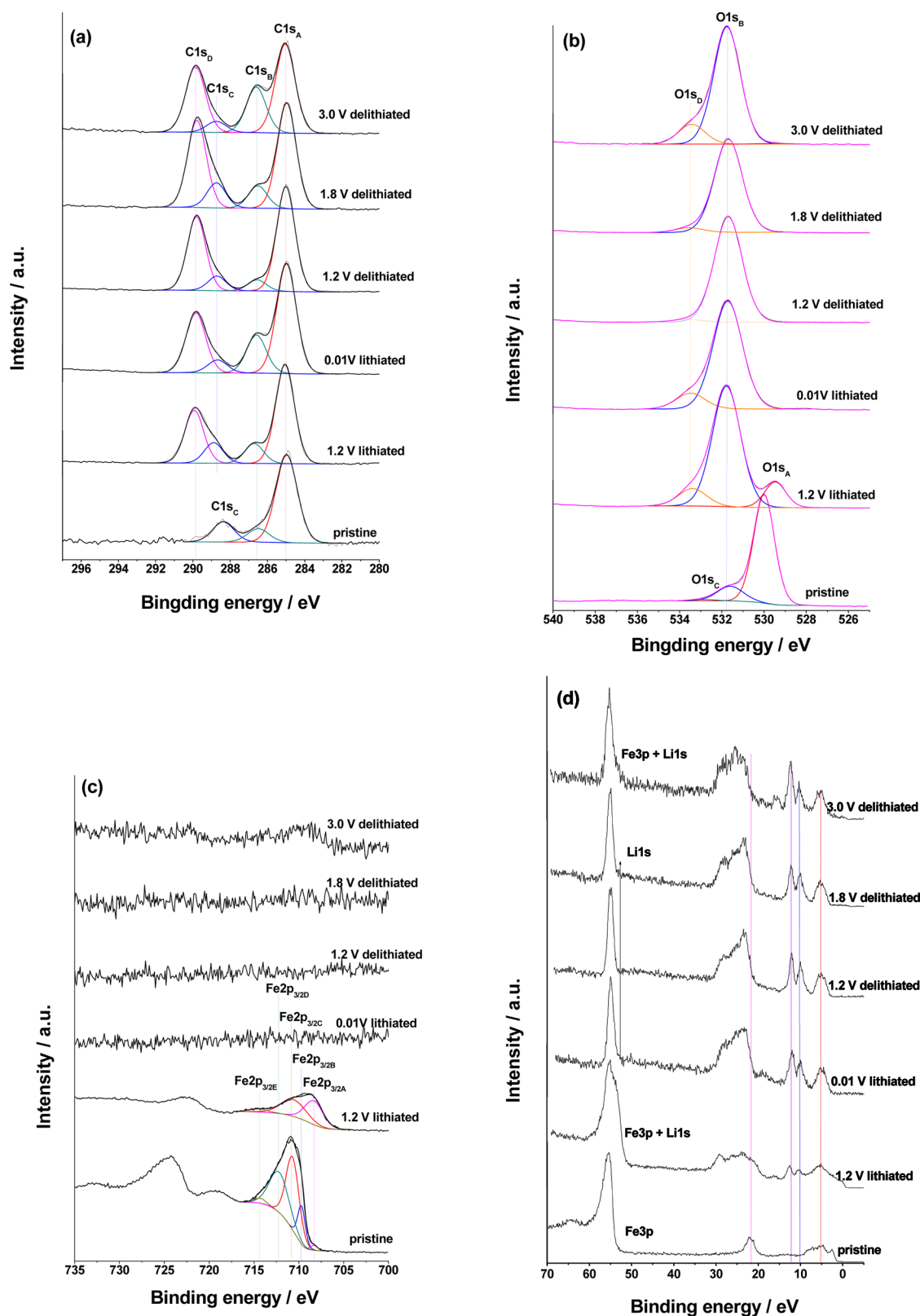


Figure 4. XP (a) C 1s, (b) O 1s, and (c) Fe 2p core levels and (d) Fe 3p–Li 1s core levels and VB region spectra for the pristine iron oxide thin film and samples treated at selected potentials in the first lithiation/delithiation cycle in 1 M LiClO₄–PC.

The formation of Fe(II) is confirmed by the enlargement at a lower binding energy of the Fe 3p–Li 1s peak between 50 and 60 eV. Thus, both the CV data and the XP O 1s, Fe 2p, and Fe 3p–Li 1s spectra are consistent with the intercalation of lithium

in the iron oxide matrix at 1.2 V. According to Larcher's work on Fe₂O₃ nanoparticles, there is less than 2 mol of Li per Fe₂O₃ intercalated into the electrode at this stage.¹⁹ Here, Li_{1.03}Fe₂O₃ is deduced from the relative intensity of the two iron com-

Table 1. Binding Energies (E_B), Full Widths at Half-Maximum (fwhm), and Relative Intensity of the XPS Component Peaks Obtained by Peak Fitting for the Samples Lithiated/Delithiated to Different Potentials

	pristine			1.2 V lithiated			0.01 V lithiated			1.2 V delithiated			1.8 V delithiated			3.0 V delithiated		
	E_B (eV)	fwhm (eV)	area ratio	E_B (eV)	fwhm (eV)	area ratio	E_B (eV)	fwhm (eV)	area ratio	E_B (eV)	fwhm (eV)	area ratio	E_B (eV)	fwhm (eV)	area ratio	E_B (eV)	fwhm (eV)	area ratio
C 1s _A	285.0	1.41	1.00	285.0	1.24	1.00	285.0	1.29	1.00	285.0	1.20	1.00	285.0	1.23	1.00	285.0	1.29	1.00
C 1s _B	286.5	1.41	0.15	286.7	1.24	0.20	286.6	1.29	0.35	286.6	1.20	0.11	286.5	1.23	0.21	286.6	1.29	0.51
C 1s _C	288.4	1.41	0.23	288.9	1.24	0.21	288.7	1.29	0.12	288.7	1.20	0.14	288.7	1.23	0.24	288.7	1.29	0.12
C 1s _D				289.9	1.24	0.53	289.9	1.29	0.55	289.8	1.20	0.71	289.8	1.23	0.82	289.8	1.29	0.74
O 1s _A	530.0	1.21	1.00	529.5	1.23	0.16	531.7	1.70	1.00	531.7	1.61	1.00	531.7	1.61	1.00	529.5	1.54	0.01
O 1s _B	531.6	1.51	0.17	531.8	1.63	1.00										531.8	1.54	1.00
O 1s _C	532.8	1.51	0.01															
O 1s _D				533.4	1.63	0.14	533.5	1.70	0.15	533.6	1.61	0.02	533.6	1.61	0.05	533.4	1.54	0.17
Fe 2p _{3/2A}	708.3	0.96	0.04	708.3	2.51	1.00												
Fe 2p _{3/2B}	709.7	1.02	0.30															
Fe 2p _{3/2C}	710.7	1.77	1.00	710.6	3.36	0.95												
Fe 2p _{3/2D}	712.2	2.63	0.82															
Fe 2p _{3/2E}	714.3	1.56	0.06	714.5	2.50	0.12												

ponents (Fe(II)/Fe(III) = 1.00/0.95), a value consistent with Li intercalation in the Fe₂O₃ thin-film matrix.

After lithiation to 0.01 V, the Fe 2p intensity is completely attenuated by the growth of the SEI layer, like observed for other anode materials in the lithiated state.^{5,17,49} Consistently, full attenuation of the O 1s_A component and Fe 3p peak is also observed (only a sharp Li 1s peak is observed at about 55 eV). The SEI layer can be estimated to be at least 10 nm thick. The XP C 1s and O 1s core levels show no major change of the SEI layer composition, still dominated by the presence of Li₂CO₃ and with ROCO₂Li as the minor constituent. In the VB region, different features can be distinguished. The composite peak between 20 and 30 eV can be assigned to the O 2s band. For the pristine sample, a much narrower peak at ~21–22 eV can be attributed to O 2s from the iron oxide. Similarly, the composite peak observed between 3 and 8 eV on the pristine sample corresponds to the O 2p band from iron oxide. For the sample lithiated at 1.2 V, these peaks are overlapped with peaks that can be assigned to carbonate anion molecular orbitals (MOs). After lithiation to 0.01 V, the composite peaks at 20–30 eV and 3–8 eV correspond entirely to MOs of carbonate. New peaks at ~10.0 and ~13.0 eV are representative of the C–O bond in Li₂CO₃.^{50,51} The presence of Li₂CO₃ is thus confirmed to be the major component of the SEI layer like observed on other anode materials in the lithiated state.^{5,11,17,18}

After delithiation at 1.2 and 1.8 V, the XP Fe 2p and Fe 3p core levels are still fully attenuated by the SEI layer, which precludes any discussion of the deconversion mechanism. Only after delithiation at 3.0 V, some signals arise in the Fe 2p region, confirming further decomposition of the SEI layer in this later stage of the delithiation process. Consistently, the Fe 3p–Li 1s peak is lightly enlarged at higher binding energy. This phenomenon has also been reported for carbon materials⁵² and rutile TiO₂.⁴⁹ The C 1s and O 1s spectra show that no additional species appears in the SEI layer during the delithiation process. Only the relative intensities of the component peaks slightly vary, indicating small variations in the proportions of the constituents. The VB region remains quite similar to that observed in the lithiated state at 0.01 V. Thus, XPS is consistent with the EIS data showing that only partial decomposition of the SEI layer occurs upon delithiation until 3.0 V. In addition, it shows that the SEI layer composition remains dominated by Li₂CO₃ during the whole lithiation/delithiation process. The dominant components of the SEI layer can vary as a function of salt (i.e., LiPF₆) and solvent (mixture of carbonates) used in electrolytes.⁵³

3.5. XPS Depth Profile Analysis of Sample Lithiated at 0.01 V. Figure 5 presents the XP C 1s, O 1s, Fe 2p, and Fe 3p–Li 1s core levels and VB region spectra of the sample lithiated to 0.01 V for increasing Ar⁺ sputtering time. The E_B and fwhm values and relative intensities of the component peaks are compiled in Table 2. As discussed above, C 1s and O 1s spectra before sputtering are indicative of the composition (Li₂CO₃ and ROCO₂Li) of the SEI layer formed at the surface of the electrode. The photoelectrons emitted by the converted electrode are fully attenuated by the SEI surface layer, and as a consequence, the Fe 3p–Li 1s core level and VB (3–30 eV) spectra are characteristic of the SEI layer (no Fe 3p component).

After 2 min Ar⁺ sputtering (about 5 nm etched), the C 1s_A component markedly decreases in intensity, indicating removal of the outer part of the surface carbonaceous layer mostly consisting of hydrocarbons. The decrease of the relative intensity of the O 1s_C component indicates that ROCO₂Li species are also

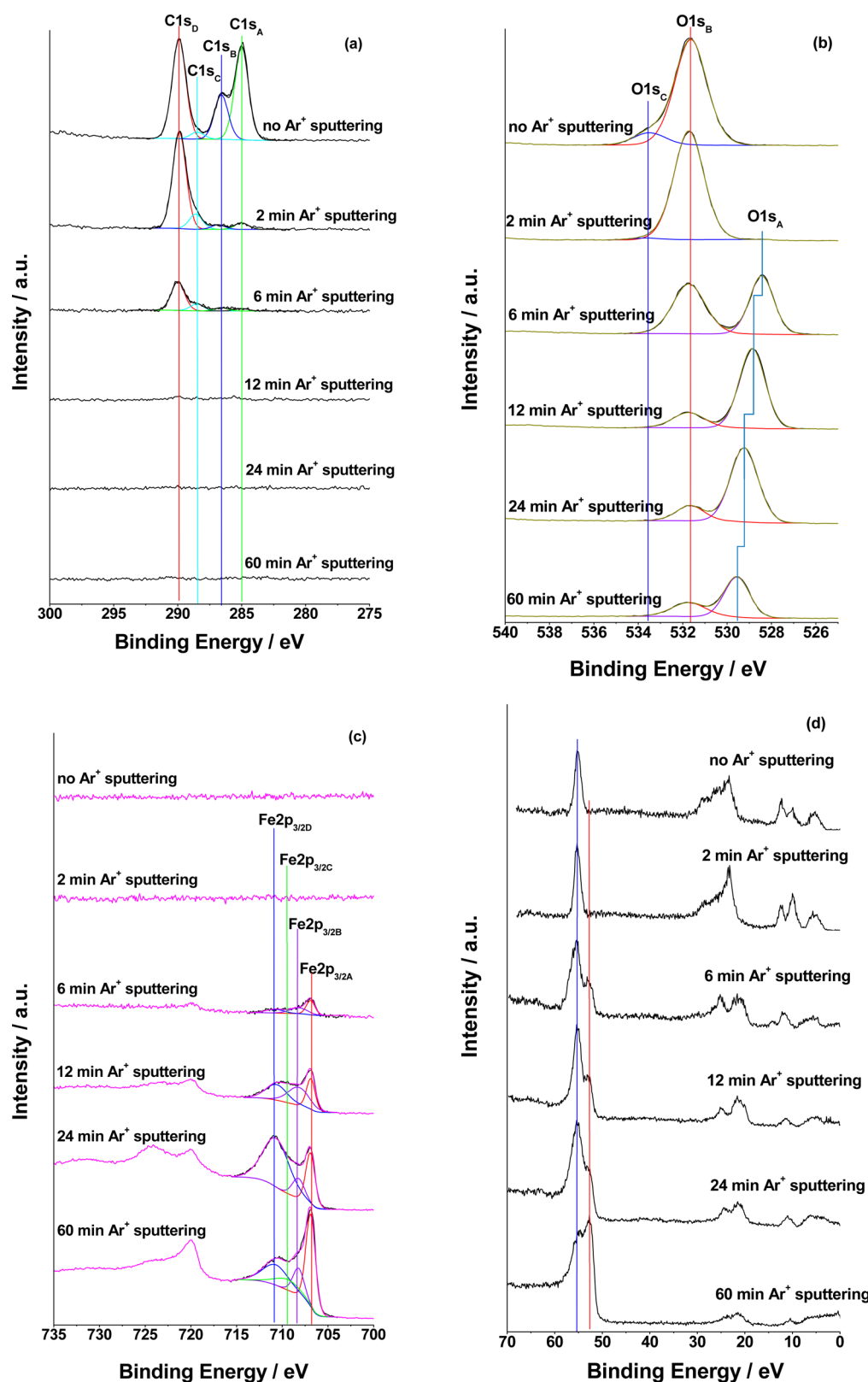


Figure 5. XP (a) C 1s, (b) O 1s, and (c) Fe 2p core levels and (d) Fe 3p–Li 1s core levels and VB region spectra of the sample lithiated to 0.01 V for increasing Ar^+ sputtering time.

preferentially removed. Complete attenuation of the Fe 2p intensity is still observed indicating that profiling is still in the bulk SEI layer region. Consistently, the Fe 3p–Li 1s core level and VB (3–30 eV) spectra are still those of the SEI layer with

slight changes in the relative intensities of the VB caused by removal of the outermost hydrocarbons.

After 6 min Ar^+ sputtering, a metallic iron Fe(0) component at 706.9 eV along with lower intensity Fe(II) and Fe(III) oxide

Table 2. Binding Energies (E_B), Full Widths at Half-Maximum (fwhm), and Relative Intensity of the XPS Component Peaks Obtained by Peak Fitting for the Sample Lithiated to 0.01 V as a Function of Depth Sputtering Time

	0.01 V lithiated				2 min V sputtering				6 min V sputtering				12 min V sputtering				24 min V sputtering				60 min V sputtering			
	E_B (eV)	fwhm (eV)	area ratio	E_B (eV)	fwhm (eV)	area ratio	E_B (eV)	fwhm (eV)	area ratio	E_B (eV)	fwhm (eV)	area ratio	E_B (eV)	fwhm (eV)	area ratio	E_B (eV)	fwhm (eV)	area ratio	E_B (eV)	fwhm (eV)	area ratio	E_B (eV)	fwhm (eV)	area ratio
C 1s _A	285.0	1.31	0.94	285.0	1.28	0.07	285.0	1.27	0.09															
C 1s _B	286.6	1.31	0.44	286.8	1.28	0.05	286.6	1.27	0.11															
C 1s _C	288.5	1.31	0.07	288.6	1.28	0.16	288.5	1.27	0.24															
C 1s _D	289.9	1.31	1.00	290.0	1.28	1.00	290.0	1.27	1.00															
O 1s _A							528.4	1.33	0.87	528.9	1.40	1.00	529.2	1.51	1.00	529.6	1.38	1.00						
O 1s _B	531.6	1.76	1.00	531.7	1.65	1.00	531.7	1.79	1.00	531.7	1.74	0.24	531.7	1.53	0.21	531.7	1.88	0.47						
O 1s _C	533.5	1.76	0.12	533.7	1.65	0.02																		
Fe 2p _A							706.9	1.16	1.00	706.9	1.19	0.73	706.9	1.23	0.38	706.9	1.28	1.00						
Fe 2p _B							708.2	2.35	0.85	708.3	2.93	1.00	708.2	1.65	0.19	708.2	1.53	0.35						
Fe 2p _C																								
Fe 2p _D							710.8	2.35	0.54	710.7	2.93	0.87	710.7	3.50	1.00	710.7	3.47	0.59						

components at 708.2 and 710.8 eV, respectively, and an oxide O 1s_A component at 528.4 eV are detected. Consistently, a Fe 3p contribution is observed at lower binding energy in the Fe 3p–Li 1s core level spectrum, and the VB spectrum region is changed. The principal modifications of the VB spectrum are the appearance of a new component at ~21 eV attributed to O 2s from the iron oxide as discussed above and the disappearance of a component at ~10 eV attributed to the carbonate anion MO. At the same time, the intensity of the C 1s_D component at 290.0 eV has markedly decreased, and that of the C 1s_A component at 285.0 eV almost disappeared. This means that most of the SEI layer and almost all surface hydrocarbons were removed. According to the Ar⁺ sputtering rate, about 15 nm of material was sputtered, which gives an approximation of the thickness of the SEI layer formed on the electrode surface lithiated at 0.01 V in LiClO₄–PC. Small nitrogen peaks (NO₂ and/or NO components, not shown) were detected, indicating surface contamination brought by Ar⁺ sputtering. The fact that both metallic and iron oxide components are measured points to partial conversion of the thin-film material.

After 12 min Ar⁺ sputtering, the C 1s core level shows nearly no intensity anymore, indicating full removal of the surface SEI layer. For binding energy calibration and for consistent comparison, the binding energy of the O 1s_B peak (C=O and/or N=O bonds) was set at 531.7 eV. It is then clearly seen that the lower binding energy O 1s_A peak of metal oxides shifts from 528.4 to 528.9 eV, which is consistent with a component change of metal oxides from lithium oxides to iron oxides. Consistently with the removal of the SEI layer, the intensity of the Fe 2p core level increases as well as that of the Fe 3p–Li 1s core level with displacement of this composite peak to lower binding energies. The relative intensity of the Fe(0) component remains high, indicating that profiling is still in the converted region of the iron oxide film. However, the increasing relative intensity of the Fe(III) components indicates that profiling approaches the unconverted inner part of the thin film.

After 24 min Ar⁺ sputtering, the Fe(III) peak at 710.7 eV becomes the dominant component of the Fe 2p_{3/2} core level spectrum, showing the characteristics of the pristine iron oxide film (O 1s_A peak further shifted to 529.2 eV). This means that profiling has further approached an unconverted (or partly converted) region in the inner part of the thin film as confirmed by the ToF-SIMS results presented below. After 60 min Ar⁺ sputtering (corresponding to about 150 nm of thickness), the markedly enhanced metallic Fe(0) peak at 706.9 eV and decreased intensity of the O 1s_A peak indicate that the substrate region has been reached with only traces of the original iron oxide film remaining. This is confirmed by the change of the shape of the Fe 3p–Li 1s peak. The marker peaks characteristic of the MOs of carbonate anion are no longer observed. The low intensity peak at ~21 eV and large peak between 3 and 8 eV correspond to O 2s and O 2p bands, respectively, from the remaining iron oxide traces.

3.6. ToF-SIMS Depth Profiles Analysis of Pristine, Lithiated, And Delithiated Samples. Figure 6 shows the negative ion depth profiles of the Li-containing ions (Li⁺, LiO[−]) and Fe-containing ions (FeO[−], FeO₂[−], Fe₂[−], Fe₂O₃[−], Fe₃O₄[−]) of the pristine, lithiated (to 0.01 V), and delithiated (to 3.0 V) samples. All profiles were recorded in the same conditions to allow direct comparison between samples. The intensity is presented using a logarithmic scale to magnify the low intensity signals. The ion intensity modifications with sputtering time

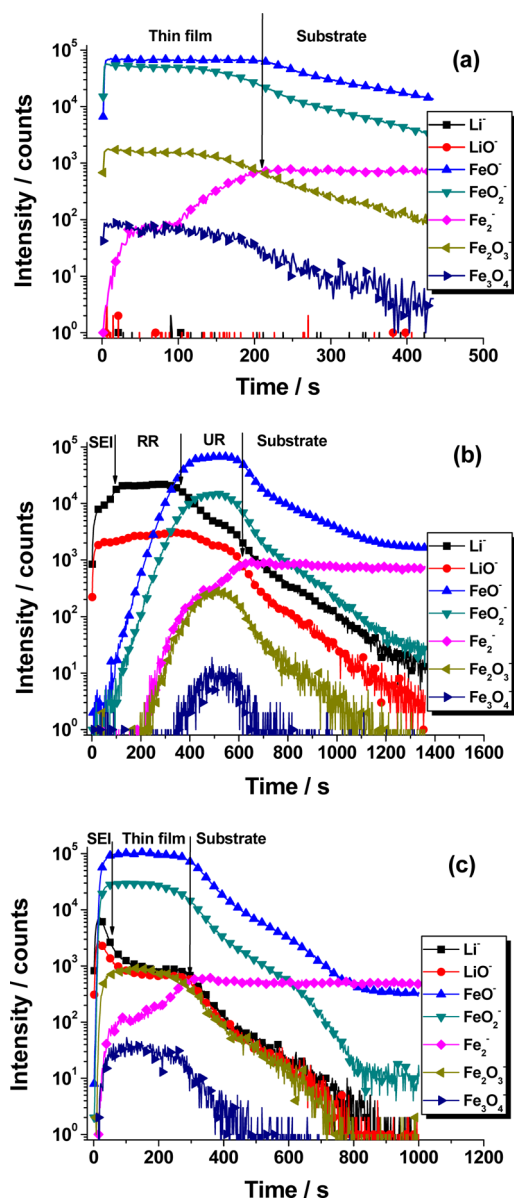


Figure 6. ToF-SIMS negative ion depth profiles of (a) the pristine, (b) lithiated to 0.01 V, and (c) delithiated to 3.0 V samples.

reflect the in-depth variations of concentration but are also dependent on the matrix from which the ions are emitted.

For the pristine sample (Figure 6(a)), extremely low intensity Li-containing ion profiles are shown for comparison with the electrochemically treated samples discussed below. Several regions can be distinguished from the depth profiles of the Fe-containing ions. At the beginning of sputtering, all ion intensities increase for a few seconds to reach stationary conditions. After about 5 s, a plateau characterizes the variation of the FeO^- , FeO_2^- , Fe_2O_3^- , and Fe_3O_4^- ion profiles. It corresponds to the bulk region of the iron oxide film. The Fe_2^- ion curve shows a gradual increase from ~ 100 to ~ 210 s, corresponding to the transition from the mixed higher valent ($\text{Fe}^{3+}/\text{Fe}^{2+}$, as shown by XPS and Raman) iron oxide region to the metallic substrate region and thus marking the interfacial region between oxide film and substrate. After about 120 s, the intensities of the FeO_2^- , Fe_2O_3^- , and Fe_3O_4^- ions start to decrease slowly, whereas that of the FeO^- ions remains stable. This is consistent with the predominance of lower valent (Fe^{2+})

iron ions in the inner part of the oxide film at the interface with the substrate. After about 210 s sputtering, the Fe_2^- ions are stable in intensity, confirming that the iron substrate region is reached.

For the sample lithiated to 0.01 V (Figure 6(b)), the sputtering time to reach the substrate region has increased to about 610 s, which is almost 3 times that of the pristine sample. Undoubtedly, the prolonged sputtering time reflects swelling of the iron oxide thin film caused by volume expansion during the lithiation process. However, it does not mean that the thickness of the lithiated oxide layer has tripled because a matrix effect can affect the sputtering yield. Actually, the theoretical expansion for the conversion reaction 1 is 193% as deduced from molar volume calculation ($30.5 \text{ cm}^3/\text{mol}$ for Fe_2O_3 , $7.1 \text{ cm}^3/\text{mol}$ for Fe, and $14.84 \text{ cm}^3/\text{mol}$ for Li_2O). Such a volume expansion is expected to fracture the oxide thin film, which may be one reason for the inferior cycling performance of this kind of material. Indeed, large volume changes induced by cycling have been reported to fracture a large hematite particle in contrast to nanorods which undergo only pulverization but no electrode damage.⁵⁴

According to the XPS data presented above, the thickness expansion for the sample lithiated to 0.01 V can be estimated to about 170% ($150 \text{ nm}/(85\text{--}95 \text{ nm})$), which is slightly lower than the theoretical value of volume expansion and consistent with an incomplete conversion of the thin-film electrode, also shown by the XPS.

The SEI layer region has a width of ~ 80 s in sputtering time (from ~ 20 to ~ 100 s). The interface between the SEI layer and the converted oxides is well marked by the Li-containing ions (Li^- , LiO^-). Under the SEI layer, a plateau with a stable intensity of the Li-containing ions is observed, which can be assigned to the main converted region of the oxide film (reacted region, RR in Figure 6(b)). The intensities of the Fe-containing ions (FeO^- , FeO_2^- , Fe_2O_3^- , Fe_3O_4^-) are quite low compared to those for the pristine sample, indicating a high conversion ratio in this main reacted region. After ~ 360 s, the intensities of the Fe-containing ions (FeO^- , FeO_2^- , Fe_2O_3^- , Fe_3O_4^-) reach their maximum. The intensity of FeO^- ions in this region is similar to that for the pristine oxide sample, but the intensities of FeO_2^- , Fe_2O_3^- , and Fe_3O_4^- ions are 1 order of magnitude smaller than for the pristine sample. In this inner unreacted region (UR in Figure 6(b)) at the interface with the current collector (substrate), the iron oxide film is partially lithiated, possibly to lower valence Fe(II) oxides, which is further supported by the slowly declining intensities of the Li-containing ions. This stratification of the iron oxide film into a fully lithiated outer part and a partially lithiated inner part most likely results from the limitation of the lithiation reaction by mass transport, like previously observed for Cr_2O_3 and Sn–Co and Sn–Ni alloys.^{5,17,18}

For the sample delithiated to 3.0 V (Figure 6(c)), the sputtering time to reach the substrate has decreased to about 300 s, reflecting volume shrinking upon delithiation. However, this value is higher than for the pristine film, which is a first indication of a non-fully-reversible lithiation process. The Fe-containing ions (FeO^- , FeO_2^- , Fe_2O_3^- , Fe_3O_4^-) display a plateau from ~ 55 to ~ 300 s of sputtering, which is assigned to deconversion of Fe with Li_2O to form Fe_2O_3 (reaction 3). It seems that the main reaction region (RR) in the 0.01 V lithiated sample has disappeared, indicating reaction and diffusion of Li^+ ions in and out of the film. Compared to the 0.01 V lithiated sample, the profiles of Li-containing ions (Li^- , LiO^-) display higher intensities for a shorter sputtering time before decreasing to a lower plateau level, indicating a delithiation process of Li^+ ions

through the SEI layer. The narrower region of high intensities of the Li-containing ions (~ 55 vs ~ 80 s in the lithiated state) is attributed to the SEI layer, which is partially decomposed after deconversion, in agreement with the EIS and XPS data. In contrast to the pristine sample, Li-containing ions are markedly present in the delithiated sample. This evidences that there is some lithium trapped in the deconverted oxide, indicating that the process is not totally reversible. This points to a delithiation process being mainly limited by mass transport to the electrolyte/oxide interface as observed above for the lithiation process. This was also observed previously for Cr_2O_3 .⁵

4. CONCLUSIONS

Surface and depth profile analysis (XPS and ToF-SIMS) was combined with electrochemical techniques (CV and EIS) to study the lithiation/delithiation mechanism of iron oxide as anode material for LiBs. A thin-film model electrode was prepared by a simple thermal oxidation process at 300°C in air of pure iron substrate, used as a current collector. Raman, XPS, and ToF-SIMS showed that the oxide film consists of Fe(III) ions forming an $\alpha\text{-Fe}_2\text{O}_3$ phase in majority with lower valent Fe(II) ions forming a Fe_3O_4 phase in the inner part of the film at the interface with the current collector.

The SEI layer formed by reductive decomposition of the $\text{LiClO}_4\text{-PC}$ electrolyte on the iron oxide thin-film electrode is mainly constituted of Li_2CO_3 with ROCO_2Li as a minor constituent, independently of the lithiation/delithiation of the electrode. It was shown here for the first time that the thickness of the SEI layer formed on the surface of conversion-type metallic oxide electrode material evolves upon the lithiation/delithiation process. After lithiation to 1.2 V (i.e., before conversion occurring at 0.75 V), Li intercalates in the $\alpha\text{-Fe}_2\text{O}_3$ matrix to form $\text{Li}_{1.03}\text{Fe}_2\text{O}_3$ as measured by XPS. The SEI layer is already formed at this stage. After lithiation to 0.01 V, the SEI layer grows in thickness to at least 15 nm. The thin-film electrode approach allowed us to show that the conversion reaction leading to formation of metallic Fe and Li_2O is accompanied by material swelling, except in its inner part where an unconverted and/or partially converted material subsists due to limitation of the conversion reaction by mass transport. Deconversion, occurring at ~ 1.55 V, is not totally reversible and also limited by mass transport. It causes shrinking of the electrode material with lithium trapped in the deconverted part. The SEI layer mostly decomposes and reduces in thickness above 1.8 V, i.e., after the main deconversion reaction.

AUTHOR INFORMATION

Corresponding Author

*E-mail: jolanta-swiatowska@chimie-paristech.fr.

Notes

The authors declare no competing financial interest.

ACKNOWLEDGMENTS

Region Ile-de-France is acknowledged for partial support for the ToF-SIMS and XPS equipment. Bingbing Tian thanks the China Scholarship Council for his PhD scholarship. The authors thank Dr. Zhesheng Chen for Raman spectroscopy analysis.

REFERENCES

- (1) Poizot, P.; Laruelle, S.; Grugeon, S.; Dupont, L.; Tarascon, J.-M. Nano-sized Transition-Metal Oxides as Negative-Electrode Materials for Lithium-Ion Batteries. *Nature* **2000**, *407*, 496–499.
- (2) Wang, G. X.; Chen, Y.; Konstantinov, K.; Lindsay, M.; Liu, H. K.; Dou, S. X. Investigation of Cobalt Oxides as Anode Materials for Li-ion Batteries. *J. Power Sources* **2002**, *109*, 142–147.
- (3) Aricò, A. S.; Bruce, P.; Scrosati, B.; Tarascon, J.-M.; Schalkwijk, W. V. Nanostructured Materials for Advanced Energy Conversion and Storage Devices. *Nat. Mater.* **2005**, *4*, 366–377.
- (4) Taberna, P. L.; Mitra, S.; Poizot, P.; Simon, P.; Tarascon, J.-M. High Rate Capabilities Fe_3O_4 -based Cu Nano-architected Electrodes for Lithium-ion Battery Applications. *Nat. Mater.* **2006**, *5*, 567–573.
- (5) Li, J. T.; Maurice, V.; Światowska-Mrowiecka, J.; Seyeux, A.; Zanna, S.; Klein, L.; Sun, S. G.; Marcus, P. XPS, Time-of-Flight-SIMS and Polarization Modulation IRRAS Study of Cr_2O_3 Thin Film Materials as Anode for Lithium Ion Battery. *Electrochim. Acta* **2009**, *54*, 3700–3707.
- (6) Wen, C. J.; Huggins, R. A. Thermodynamic Study of the Lithium-Tin System. *J. Electrochem. Soc.* **1981**, *128*, 1181–1187.
- (7) Winter, M.; Besenhard, J. O. Electrochemical Lithiation of Tin and Tin-Based Intermetallics and Composites. *Electrochim. Acta* **1999**, *45*, 31–50.
- (8) Nobili, F.; Mancini, M.; Dsoke, S.; Tossici, R.; Marassi, R. Low-Temperature Behavior of Graphite–Tin Composite Anodes for Li-ion Batteries. *J. Power Sources* **2010**, *195*, 7090–7097.
- (9) Lai, S. C. Solid Lithium-Silicon Electrode. *J. Electrochem. Soc.* **1976**, *123*, 1196–1197.
- (10) Sharma, R. A.; Seefurth, R. N. Thermodynamic Properties of the Lithium-Silicon System. *J. Electrochem. Soc.* **1976**, *123*, 1763–1768.
- (11) Pereira-Nabais, C.; Światowska, J.; Chagnes, A.; Ozanam, F.; Gohier, A.; Tran-Van, P.; Cojocaru, C.-S.; Cassir, M.; Marcus, P. Interphase Chemistry of Si Electrodes Used as Anodes in Li-ion Batteries. *Appl. Surf. Sci.* **2013**, *266*, 5–16.
- (12) Philippe, B.; Dedryvère, R.; Allouche, J.; Lindgren, F.; Gorgoi, M.; Rensmo, H.; Gonbeau, D.; Edström, K. Nanosilicon Electrodes for Lithium-ion Batteries: Interfacial Mechanisms Studied Hard and Soft X-Ray Photoelectron Spectroscopy. *Chem. Mater.* **2012**, *24*, 1107–1115.
- (13) Cui, Z.; Gao, F.; Cui, Z.; Qu, J. A Second Nearest-Neighbor Embedded Atom Method Interatomic Potential for Li–Si Alloys. *J. Power Sources* **2012**, *207*, 150–159.
- (14) Weydanz, W. J.; Wohlfahrt-Mehrens, M.; Huggins, R. A. A Room Temperature Study of the Binary Lithium–Silicon and the Ternary Lithium–Chromium–Silicon System for Use in Rechargeable Lithium Batteries. *J. Power Sources* **1999**, *81–82*, 237–242.
- (15) Jayaprakash, N.; Kalaiselvi, N.; Doh, C. H. A New Class of Tailor-Made $\text{Fe}_{0.92}\text{Mn}_{0.08}\text{Si}_2$ Lithium Battery Anodes: Effect of Composite and Carbon Coated $\text{Fe}_{0.92}\text{Mn}_{0.08}\text{Si}_2$ Anodes. *Intermetallics* **2007**, *15*, 442–450.
- (16) Kamali, A. R.; Fray, D. J. Tin-Based Materials as Advanced Anode Materials for Lithium Ion Batteries: a Review. *Rev. Adv. Mater. Sci.* **2011**, *27*, 14–24.
- (17) Li, J. T.; Światowska, J.; Seyeux, A.; Huang, L.; Maurice, V.; Sun, S. G.; Marcus, P. XPS and ToF-SIMS Study of Sn–Co Alloy Thin Films as Anode for Lithium Ion Battery. *J. Power Sources* **2010**, *195*, 8251–8257.
- (18) Li, J. T.; Światowska, J.; Maurice, V.; Seyeux, A.; Huang, L.; Sun, S. G.; Marcus, P. XPS and ToF-SIMS Study of Electrode Processes on Sn–Ni Alloy Anodes for Li-Ion Batteries. *J. Phys. Chem. C* **2011**, *115*, 7012–7018.
- (19) Thackeray, M. M.; David, W. I. F.; Goodenough, J. B. High-Temperature Lithiation of $\alpha\text{-Fe}_2\text{O}_3$: A Mechanistic Study. *J. Solid State Chem.* **1984**, *55*, 280–286.
- (20) Larcher, D.; Masquelier, C.; Bonnin, D.; Chabre, Y.; Mason, V.; Leriche, J. B.; Tarascon, J.-M. Effect of Particle Size on Lithium Intercalation into $\alpha\text{-Fe}_2\text{O}_3$. *J. Electrochem. Soc.* **2003**, *150*, A133–A139.
- (21) Larcher, D.; Bonnin, D.; Cortes, R.; Rivals, I.; Personnaz, L.; Tarascon, J.-M. Combined XRD, EXAFS, and Mössbauer Studies of the Reduction by Lithium of $\alpha\text{-Fe}_2\text{O}_3$ with Various Particle Sizes. *J. Electrochem. Soc.* **2003**, *150*, A1643–A1650.
- (22) Cherian, C. T.; Sundaramurthy, J.; Kalaivani, M.; Ragupathy, P.; Suresh Kumar, P.; Thavasi, V.; Reddy, M. V.; Sow, C. H.; Mhaisalkar, S. G.; Ramakrishna, S.; et al. Electrospun $\alpha\text{-Fe}_2\text{O}_3$ Nanorods as A Stable, High Capacity Anode Material for Li-ion Batteries. *J. Mater. Chem.* **2012**, *22*, 12198–12204.

- (23) Reddy, M. V.; Yu, T.; Sow, C. H.; Shen, Z. X.; Lim, C. T.; Subba Rao, G. V.; Chowdari, B. V. R. α -Fe₂O₃ Nanoflakes as an Anode Material for Li-Ion Batteries. *Adv. Funct. Mater.* **2007**, *17*, 2792–2799.
- (24) Mitra, S.; Poizot, P.; Finke, A.; Tarascon, J.-M. Growth and Electrochemical Characterization versus Lithium of Fe₃O₄ Electrodes Made by Electrodeposition. *Adv. Funct. Mater.* **2006**, *16*, 2281–2287.
- (25) Światowska-Mrowiecka, J.; Maurice, V.; Zanna, S.; Klein, L.; Marcus, P. XPS Study of Li Ion Intercalation in V₂O₅ Thin Films Prepared by Thermal Oxidation of Vanadium Metal. *Electrochim. Acta* **2007**, *52*, 5644–5653.
- (26) Beattie, I. R.; Gilson, T. R. The Single-Crystal Raman Spectra of Nearly Opaque Materials. Iron(III) Oxide and Chromium(III) Oxide. *J. Chem. Soc. A* **1970**, *5*, 980–986.
- (27) Zheng, Z.; Chen, Y.; Shen, Z. X.; Ma, J.; Sow, C. H.; Huang, W.; Yu, T. Ultra-Sharp α -Fe₂O₃ Nanoflakes: Growth Mechanism and Field-Emission. *Appl. Phys. A: Mater. Sci. Process.* **2007**, *89*, 115–119.
- (28) Faria, D. L. A.; Venâncio Silva, S.; Oliveira, M. T. Raman Microspectroscopy of Some Iron Oxides and Oxyhydroxides. *J. Raman Spectrosc.* **1997**, *28*, 873–878.
- (29) Bellot-Gurlet, L.; Neff, D.; Réguer, S.; Monnier, J.; Saheb, M.; Dillmann, P. Raman Studies of Corrosion Layers Formed on Archaeological Irons in Various Media. *J. Nano Res.* **2009**, *8*, 147–156.
- (30) Laruelle, S.; Grugeon, S.; Poizot, P.; Dolle, M.; Dupont, L.; Tarascon, J.-M. On the Origin of the Extra Electrochemical Capacity Displayed by MO/Li Cells at Low Potential. *J. Electrochem. Soc.* **2002**, *149*, A627–A634.
- (31) Hosono, E.; Fujihara, S.; Honma, I.; Ichihara, M.; Zhou, H. Fabrication of Nano/Micro Hierarchical Fe₂O₃/Ni Micrometer-Wire Structure and Characteristics for High Rate Li Rechargeable Battery. *J. Electrochem. Soc.* **2006**, *153*, A1273–A1278.
- (32) Nuli, Y. N.; Zeng, R.; Zhang, P.; Guo, Z. P.; Liu, H. K. Controlled Synthesis of α -Fe₂O₃ Nanostructures and Their Size-Dependent Electrochemical Properties for Lithium-Ion Batteries. *J. Power Sources* **2008**, *184*, 456–461.
- (33) Chaudhari, S.; Srinivasan, M. 1D Hollow α -Fe₂O₃ Electrospun Nanofibers as High Performance Anode Material for Lithium Ion Batteries. *J. Mater. Chem.* **2012**, *22*, 23049–23056.
- (34) Thevenin, J. Passivating Films on Lithium Electrodes. An Approach by Means of Electrode Impedance Spectroscopy. *J. Power Sources* **1985**, *14*, 45–52.
- (35) Levi, M. D.; Aurbach, D. Diffusion Coefficients of Lithium Ions during Intercalation into Graphite Derived from the Simultaneous Measurements and Modeling of Electrochemical Impedance and Potentiostatic Intermittent Titration Characteristics of Thin Graphite Electrodes. *J. Phys. Chem. B* **1997**, *101*, 4641–4647.
- (36) Shin, H. C.; Cho, W.; Jang, H. Electrochemical Properties of the Carbon-Coated LiFePO₄ as a Cathode Material for Lithium-ion Secondary Batteries. *J. Power Sources* **2006**, *159*, 1383–1388.
- (37) Yang, Y.; Wang, C.; Yue, B.; Gambhir, S.; Too, C. O.; Wallace, G. G. Electrochemically Synthesized Polypyrrole/Graphene Composite Film for Lithium Batteries. *Adv. Energy Mater.* **2012**, *2*, 266–272.
- (38) Lindström, R.; Maurice, V.; Groult, H.; Perrigaud, L.; Zanna, S.; Cohen, C.; Marcus, P. Li-Intercalation Behaviour of Vanadium Oxide Thin Film Prepared by Thermal Oxidation of Vanadium Metal. *Electrochim. Acta* **2006**, *51*, S001–S011.
- (39) Yang, C. R.; Song, J. Y.; Wang, Y. Y.; Wan, C. C. Impedance Spectroscopic Study for the Initiation of Passive Film on Carbon Electrodes in Lithium Ion Batteries. *J. Appl. Electrochem.* **2000**, *30*, 29–34.
- (40) Zhou, W.; Zhu, J.; Cheng, C.; Liu, J.; Yang, H.; Cong, C.; Guan, C.; Jia, X.; Jin Fan, H.; Yan, Q.; et al. A General Strategy Toward Graphene@Metal Oxide Core–Shell Nanostructures for High-Performance Lithium Storage. *Energy Environ. Sci.* **2011**, *4*, 4954–4961.
- (41) Zhao, X.; Xia, D.; Zheng, K. Fe₃O₄/Fe/Carbon Composite and Its Application as Anode Material for Lithium-Ion Batteries. *ACS Appl. Mater. Interfaces* **2012**, *4*, 1350–1356.
- (42) Li, X.; Huang, X.; Liu, D.; Wang, X.; Song, S.; Zhou, L.; Zhang, H. Synthesis of 3D Hierarchical Fe₃O₄/Graphene Composites with High Lithium Storage Capacity and for Controlled Drug Delivery. *J. Phys. Chem. C* **2011**, *115*, 21567–21573.
- (43) Lee, Y. M.; Lee, J. Y.; Shim, H. T.; Lee, J. K.; Park, J. K. SEI Layer Formation on Amorphous Si Thin Electrode during Precycling Batteries and Energy Storage. *J. Electrochem. Soc.* **2007**, *154*, A515–A519.
- (44) Światowska-Mrowiecka, J.; Maurice, V.; Zanna, S.; Klein, L.; Marcus, P. XPS Study of Li Ion Intercalation in V₂O₅ Thin Films Prepared by Thermal Oxidation of Vanadium Metal. *Electrochim. Acta* **2007**, *52*, 5644–5653.
- (45) Światowska-Mrowiecka, J.; Diesbach, S.; Maurice, V.; Zanna, S.; Klein, L.; Briand, E.; Vickridge, I.; Marcus, P. Li-Ion Intercalation in Thermal Oxide Thin Films of MoO₃ as Studied by XPS, RBS, and NRA. *J. Phys. Chem. C* **2008**, *112*, 11050–11058.
- (46) McIntyre, N. S.; Zetaruk, D. G. X-Ray Photoelectron Spectroscopic Studies of Iron Oxides. *Anal. Chem.* **1977**, *49*, 1521–1529.
- (47) Stambouli, V.; Palacio, C.; Mathieu, H. J.; Landolt, D. Comparison of In-Situ Low-Pressure Oxidation of Pure Iron at Room Temperature in O₂ and in O₂/H₂O Mixtures Using XPS. *Appl. Surf. Sci.* **1993**, *70–71*, 240–244.
- (48) Bhargava, G.; Gouzman, I.; Chun, C. M.; Ramanarayanan, T. A.; Bernasek, S. L. Characterization of The “Native” Surface Thin Film on Pure Polycrystalline Iron: A High Resolution XPS and TEM Study. *Appl. Surf. Sci.* **2007**, *253*, 4322–4329.
- (49) Bryngelsson, H.; Stjern Dahl, M.; Gustafsson, T.; Edström, K. How Dynamic Is the SEI? *J. Power Sources* **2007**, *174*, 970–975.
- (50) Dedryvère, R.; Gireaud, L.; Grugeon, S.; Laruelle, S.; Tarascon, J.-M.; Gonbeau, D. Characterization of Lithium Alkyl Carbonates by X-Ray Photoelectron Spectroscopy: Experimental and Theoretical Study. *J. Phys. Chem. B* **2005**, *109*, 15868–15875.
- (51) Coluzza, C.; Cimino, N.; Decker, F.; Di Santo, G.; Liberatore, M.; Zannoni, R.; Bertolo, M.; La Rosa, S. Surface Analyses of In–V Oxide Films Aged Electrochemically by Li Insertion Reactions. *Phys. Chem. Chem. Phys.* **2003**, *5*, 5489–5498.
- (52) Pfanztel, M.; Kubiak, P.; Jacke, S.; Dimesso, L.; Jaegermann, W.; Wohlfahrt-Mehrens, M. SEI Formation on TiO₂ Rutile. *J. Electrochem. Soc.* **2012**, *159*, A809–A814.
- (53) Verma, P.; Maire, P.; Novák, P. A Review of the Features and Analyses of the Solid Electrolyte Interphase in Li-Ion Batteries. *Electrochim. Acta* **2010**, *55*, 6332–6341.
- (54) Lin, Y.-M.; Abel, P. R.; Heller, A.; Mullins, C. B. α -Fe₂O₃ Nanorods as Anode Material for Lithium Ion Batteries. *J. Phys. Chem. Lett.* **2011**, *2*, 2885–2891.